# Solution Structure and Conformational Flexibility in the Active State of the Orange Carotenoid Protein: Part I: Small-Angle Scattering

Maksym Golub[1], Marcus Moldenhauer[2], Franz-Josef Schmitt[2], Artem Feoktystov[3], Hugo Mändar[1], Eugene Maksimov[4], Thomas Friedrich[2], and Jörg Pieper[1*]

[1] Institute of Physics, University of Tartu, 50411 Tartu, Estonia

[2] Technical University Berlin, Berlin, Germany

[3] Forschungszentrum Jülich GmbH, Jülich Centre for Neutron Science (JCNS) at Heinz Maier-Leibnitz Zentrum (MLZ), Lichtenbergstr. 1, 85748 Garching,, Germany

[4] M. V. Lomonosov Moscow State University, Moscow, Russia

*Author to whom correspondence should be addressed:

Jörg Pieper

Institute of Physics, University of Tartu, W. Ostwaldi 1, 50411 Tartu, Estonia.

phone.: +(372) 737 4627

email: pieper@ut.ee

## Abstract

Orange Carotenoid Proteins (OCPs) are photoswitchable macromolecules playing an important role in non-photochemical quenching of excess energy in cyanobacterial light-harvesting. Upon absorption of a blue photon (450-500 nm) OCPs undergo a structural change from the ground state $OCP^O$ to the active state $OCP^R$, but high-resolution structures of the active state $OCP^R$ are not yet available. Here we use small-angle scattering methods combined with simulation tools to determine low-resolution structures of the active state at low protein concentrations via two approaches: first, directly by in-situ illumination of wild-type OCP achieving a turnover to the active state of >90%, and second, by using the mutant $OCP^{W288A}$ anticipated to mimic the active state structure. Data fits assuming the shape of an ellipsoid yield three ellipsoidal radii of about 9, 29 and 51±1 Å, respectively, in the case of the ground state $OCP^O$. In the active state, however, the molecule becomes somewhat narrower with the two smaller radii being 9 and only 19±3 Å, respectively, while the third dimension of the ellipsoid is significantly elongated to 85 – 92±5 Å. Reconstitutions of the active state structure corroborate that $OCP^R$ is significantly elongated compared to the ground state $OCP^O$ and characterized by a separation of the N-terminal and C-terminal domains with unfolded N-terminal extension. By direct comparison of small-angle scattering data, we directly show that the mutant $OCP^{W288A}$ can be used as a structural analogue of the active state $OCP^R$. The small-angle experiments are repeated for $OCP^O$ and the mutant $OCP^{W288A}$ at high protein concentrations of 50-65 mg/ml required for neutron spectroscopy investigating the molecular dynamics of OCP (see accompanying paper). The results reveal that the $OCP^O$ and $OCP^{W288A}$ samples for dynamics experiments are preferentially dimeric and widely resemble the structures of the ground and active states of OCP, respectively. This enables us to properly characterize the molecular dynamics of both states of OCP in the accompanying paper.

## 1. Introduction

Many cyanobacteria employ Orange Carotenoid Proteins (OCPs) for the purpose of protecting their sensitive photosystems against the harmful effects of excess light energy in a process termed non-photochemical quenching (NPQ) of phycobilisome (PBS) antenna fluorescence [1]. OCPs are light-triggered photoswitches employing ketocarotenoids as cofactors, which undergo photoconversion from the basal, dark-adapted orange state ($OCP^O$) to the active red state ($OCP^R$) upon absorption of a blue photon (450-500 nm) [2-5]. $OCP^R$ is able to interact with phycobilisome antenna complexes to consequently quench their fluorescence, thereby preventing photodamage of the underlying photosystems by dissipating excessively absorbed light energy into heat [6]. Structurally, the about 35 kDa water-soluble OCPs are subdivided into two domains of about equal size, an N-terminal and a C-terminal domain (NTD and CTD, respectively), which almost symmetrically encapsulate a single xanthophyll molecule in a common central cavity [7, 8]. The predominant xanthophyll is 3'-hydroxy-echinenone when purified from native cyanobacteria (e.g. *Synechocystis* sp. PCC 6803 or *Arthrospira maxima*), but photoactivity is also preserved with only 4(4')-ketolated xanthophylls (either echinenone, carrying a single keto group in 4-position of the terminal ring, or the 4,4'-diketolated canthaxanthin, when expressed in appropriate *E. coli* strains), whereas insertion of β-carotene or (3,3'-hydroxylated) zeaxanthin results in non-photoconvertible protein[9]. While the $OCP^O \rightarrow OCP^R$ conversion is triggered by photon absorption [5] (albeit with very low quantum yield of ~0.2 % [10, 11] making OCP an excellent light intensity sensor over the range of ambient light intensity fluctuations), the back-conversion occurs spontaneously (thermally) even in the dark, since the $OCP^O$ state is the thermodynamically stable one. In cyanobacteria, the OCP-related NPQ is terminated by the about 16 kDa Fluorescence Recovery Protein (FRP) [12-15], which exerts a dual action by speeding up detachment of the quenching-active $OCP^R$ from the PBS and accelerating the $OCP^R \rightarrow OCP^O$ back-conversion, the latter by mainly increasing the pre-exponential factor in the Arrhenius formulation of the temperature-dependent rate constant while leaving the activation energy of the process almost unchanged [16].

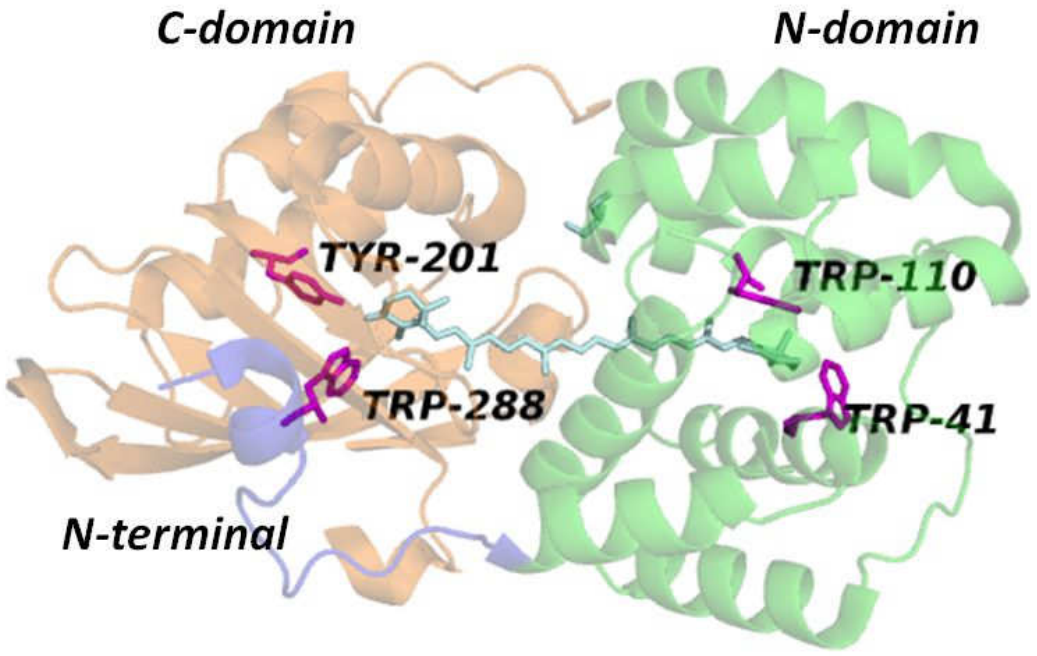


**Figure 1**: OCP$^{O}$ monomer according to the crystal structure of Leverenz et al. (pdb-code 4XB5)[17]: the N-terminal domain is shown in green, the C-terminal domain in orange, the N-terminal extension in blue and the carotenoid in cyan. The four protein residues interacting with the carotenoid are highlighted in purple color, see text.

In the basal OCP$^{O}$ state, the protein adopts a compact structure (see Fig. 1), which has been known in atomic detail for many years [7, 17, 18]. While the NTD is mainly composed of α-helices as major structural elements, the CTD is of mixed α-helical/β-sheet character and belongs to the wide-spread family of nuclear transport factor 2 (NTF-2)-like proteins (PFAM 02136). The OCP$^{O}$ structure is stabilized by multiple protein-protein interactions across the NTD-CTD interface, by the NTD-CTD linker, and by the N-terminal extension (NTE) of the NTD encompassing the αA helix that attaches to a specific site on the β-sheet surface of the CTD [19, 20]. The only specific interactions between the carotenoid and the protein are two H-bonds between the 4-keto oxygen of the carotenoid and the hydroxyl group of Tyr-201 as well as to the imino nitrogen of Trp-288 in the CTD (amino acid numbering according to *Synechocystis* sp. PCC 6803) [21, 22]. These amino acids

are highly conserved in all known OCP sequences, and mutations at either of the two positions interfere drastically with the ability to photoswitch, with carotenoid preference, with spectroscopic characteristics, or with other important physico-chemical properties of the protein. Within the NTD, Tyr-41 and Trp-110 are also in interaction distance to the other terminal ring of the carotenoid and involved in e.g. π-stacking, but mutations in these positions mostly have less severe consequences[18]. Results of a recent study employing dynamic X-ray crystallography on full-length OCP suggest that the aforementioned H-bonds are the first to break upon photoactivation. This triggers a whole series of events that eventually result in the formation of the $OCP^R$ state[10, 23, 24]. The latter is characterized by complete separation of the domains, detachment of the NTE from the CTD, and translocation of the carotenoid into the NTD [8, 17, 25]. These studies already indicate that the scheme $OCP^O \leftrightarrow OCP^R$ for the "photocycle" of OCP is an oversimplification [10]. Already in 2008, Wilson et al. [5] revealed by fs absorption spectroscopy that after decay of the excited hECN states on a ps timescale, a photoproduct remains at very low amplitude which is slightly red shifted as compared to the absorption of OCP indicating that these states of the chromophore may be similar but not identical to the state in $OCP^R$ and that subsequent relaxation of the protein takes place on timescales longer than nanoseconds. A recent multi-parametric spectroscopy study has shown that several spectroscopically discernible intermediates exist on the way, and that there is considerable asynchrony between the spectroscopic state of the carotenoid cofactor and the structural organization of the surrounding protein [24]. Thus, on the timescale of picoseconds immediately following photoexcitation [5], characteristics of the spectrally red-shifted intermediate are already observed, which is long before the large conformational changes leading to the extended configuration of the $OCP^R$ state with separated domains. On the contrary, during back-reversion, there are already spectral characteristics for some orange state, before the final structural reorganization to form the compact, dark-adapted $OCP^O$ structure comes to completion [10].

Unfortunately, a high-resolution structure of the $OCP^R$ state is still elusive, although such information would be mandatory to understand the principles of photoprotective action of the OCP protein and of its color tuning. The process of photoconversion and formation of the $OCP^R$ state eventually leads to (i) complete separation of the domains, which are only connected via the

flexible NTD-CTD linker, (ii) a large increase of the hydrodynamic volume of the protein, creating properties of a molten globule state with enhanced conformational flexibility[11], and (iii) full translocation of the carotenoid cofactor by 12 Å into the NTD [17]. Such extensive carotenoid repositioning has first been hypothesized based on the elucidation of the X-ray crystal structure of the NTD of OCP, which has previously been observed as a carotenoid-containing spontaneous hydrolysis product in native OCP preparations and was termed Red Carotenoid Protein according to its color appearance. A recent FRET triangulation study showed that this carotenoid translocation indeed occurs dynamically in the full-length OCP protein [26]. Besides the considerable disorder, the metastability of the $OCP^R$ state is problematic for high-resolution structural studies, since the protein would have to be permanently illuminated with intense blue light. However, sequence variants are already at hand, which mimic the properties of the red signaling state of OCP. One of these variants is the OCP-W288A mutant protein (initially termed "$OCP^{W288A}$" or "purple carotenoid protein"), which has been shown to have very similar hydrodynamic properties like the $OCP^R$ state, to interact with FRP and to be capable of phycobilisome fluorescence quenching without requiring photoactivation, and, therefore, should be an ideal model for the structure of the $OCP^R$ signaling state [15].

In this regard, small-angle neutron and X-ray scattering (SANS and SAXS, respectively) are valuable experimental techniques providing structural information in aqueous solution, i.e. under the same conditions as applied in spectroscopic experiments (for reviews, see [27, 28]), while neutron spectroscopy probes the molecular dynamics of biomolecules [29-31], see accompanying paper. SANS and SAXS are especially powerful in investigations in the case of complex formation out of proteins with known crystal structures [32, 33] as well as in the determination of intrinsically disordered structures like detergent micelles or belts of solubilized membrane proteins [34, 35]. Further applications in photosynthesis research (for a review see [36]) encompass neutron studies of the organization of plant thylakoid membranes in solution [37, 38], of the hydration dependence of the PS II membrane spacing [39], the structural arrangement of cyanobacterial thylakoid membranes [40, 41], but also state transitions in *Chlamydomonas reinhardtii* [42].

In the present study, we apply SANS and SAXS for investigations of the structure of the active state $OCP^R$ using two different approaches: first, via illumination of wild-type OCP, and second, employing the mutant $OCP^{W288A}$, which is expected to widely resemble the structure of $OCP^R$ see above. The results confirm that OCP undergoes a domain separation along with a considerable elongation upon illumination. Moreover, the solution structure of the mutant $OCP^{W288A}$ is shown to have a highly similar structure as $OCP^R$ in aqueous solution. Comparative neutron spectroscopy studies characterizing the molecular flexibility of OCP and of the molten globule state of $OCP^{W288A}$ on the picosecond to nanosecond timescales are reported in the accompanying paper. In the present paper, we verify that both OCP and $OCP^{W288A}$ retain their solution structures even at the relatively high protein concentrations of 50 – 65 mg/ml required for neutron spectroscopy.

## 2. Materials and Methods

**Sample Preparation: cDNA constructs and cloning:** For the expression of OCP and the pink species of the OCP-W288A mutant (PCP) we used a plasmid harboring the DNA sequence of OCP according to the published amino acid sequence (Pubmed/UniProt entry P74102) which was optimized for codon usage in E.coli by artificial gene synthesis (GeneOptimizer® algorithm, GeneArt, Life Technologies). The OCP-DNA was cloned into the first multiple cloning site of the pRSFDuet-1 vector (Novagen) by excision with BamHI and NotI. The resulting N-terminal amino acid sequence was: MGSSHHHHHHSQDPATM(1)..., which was verified by DNA sequencing (Eurofins MWG Operon, Germany). The OCP wild type protein was cloned into a modified pRSFDuet-1 vector which encodes a specific human rhinovirus 3C protease cleavage site (LEVLFQ/GP) for cleaving the His6-tag (plasmid called "pRSFDuetM"). After incubation with 3C protease the N-terminal amino acid sequence for the OCP-WT was: GPDPATM(1)… . The W288A mutant was generated by using the QuikChange® site-directed mutagenesis kit (Stratagene) according to manufacturer's instructions.

**Protein expression and purification:** For expression of the holo-protein the pRSFDuetM-OCP or pRSFDuet-PCP plasmid was transformed in echinenone producing BL21(DE3) E.coli cells (New England Biolabs). The carotenoid expression is essentially described in [22]. The expression conditions were the same for all constructs: 500 ml of medium supplemented with 34 µg/ml chloramphenicol (carotenoid producing plasmid) and 50 µg/ml kanamycin (for OCP plasmid) were inoculated from an overnight culture to an OD of 0.05 and grown in an orbital shaker at 37 °C and 220 rpm until the OD reached 0.7-0.8. After the induction with 0.5 mM IPTG the cells were grown for 48-72 h at 25 °C. Cells were harvested by centrifugation at 10,000 × g at 4 °C for 20 minutes and frozen until use.

The frozen cell pellets were resuspended in phosphate buffer (137 mM NaCl, 2.7 mM KCL, 12 mM phosphate, pH 7.4) and supplemented with 100 mg lysozyme and protease inhibitors (Complete®, Roche). The cell lysis was performed by 3-4 freeze/thaw cycles on dry ice with absolute ethanol and a water bath at room temperature. After removal of the cell debris by centrifugation (18,000 × g, 4 °C) the clarified supernatant was purified by affinity chromatography

with a peristaltic pump using 5 ml $Co^{2+}$-HiTrap Talon crude columns (GE Healthcare). The protein was eluted by an imidazole containing phosphate buffer (250 mM imidazole). After affinity chromatography either the $His_6$-tag cleavage or a hydrophobic-interaction-chromatography was performed. For cleavage with 3C protease the purified 3C protease was added in a 1:1000 dilution (referred to the total protein mass) to the eluted protein solution and incubated for 18 h at 4 °C in 3C protease buffer (20 mM Tris, 100 mM NaCl, 2 mM DTT, pH 7.5). After $His_6$-cleavage the protein solution was applied to an affinity chromatography column for the second time and the flow through was collected for dialysis in HIC buffer (500 mM $(NH_4)_2SO_4$, 100 mM NaCl, 10 mM phosphate, pH 7.4) over night at 4 °C. The hydrophobic-interaction-chromatography was carried out on a HiPrep 16/10 Phenyl HP column (Ge Healthcare) with an ÄKTA FPLC purification system (GE Healthcare). The protein was eluted using a buffer gradient with a second buffer which contained 10 mM phosphate and 100 mM NaCl. After HIC the protein was dialyzed in phosphate buffer and finally a size-exclusion-chromatography was performed on a Superdex™ 200 Increase 10/300 column (GE Healthcare). The large amount of protein that is necessary for QENS experiments was produced by using a rich minimal medium [43]. Finally, about 6 liters of MTM was used to obtain a total of 100 mg protein for QENS experiments.

**Protein preparation for QENS and SANS experiments:** The buffer was exchanged from $H_2O$ to $D_2O$ in order to suppress the solvent scattering in the case of QENS experiments and to decrease the incoherent background in the case of SANS experiments. This was achieved by using a phosphate buffer in $D_2O$ prepared by dissolving a PBS tablet (Life technologies) in 100 ml $D_2O$ (Sigma Aldrich, 99.9% D content). The purified proteins were concentrated in a centrifugation concentration filter (PALL corporation Macrosep®) to 400-500 µl and diluted with $D_2O$ phosphate buffer for 3-4 times till a $D_2O$ content of 99.9% was reached. The protein solutions were sealed in small tubes and frozen at -80 °C until use.

**Small-Angle Neutron and X-ray Scattering:** The SANS experiments on OCP and $OCP^{W288A}$ samples were carried out at the KWS-1 small-angle diffractometer (JCNS at MLZ, Garching, Germany). KWS-1 is perfectly suited to perform high-resolution measurements thanks to its 10%

wavelength spread. The neutron wavelength used in the present experiment was 5 Å. By measuring at two sample-detector distances of 8 m and 20 m, we could cover the Q range from 0.006 to 0.45 $Å^{-1}$. The samples were kept in standard 1 mm Helma cells at a constant temperature of 15 °C. We used samples in the 100% $D_2O$ contrast at two concentrations of about 64 mg/ml and 1 mg/ml, respectively. The data reduction procedure includes the correction according to detector sensitivity mask. The data treatment is carried out using the QtiKWS program [44]. More details about the KWS-1 can be found in [45].

The SAXS measurements were performed on the diffractometer SmartLabTM (Rigaku) at the Institute of Physics, University of Tartu by using the SAXS optics and CuKα radiaton (λ=1.56098 Å, rotating anode X-ray tube working at 180 mA and 45 kV, sample-detector distance of 300 mm). The program NanoSolver (Rigaku) was used to pre-process the scattering data, to subtract the buffer scattering (see sample preparation) and to correct slit smearing effects.

SANS/SAXS data analysis

The small-angle scattering from a diluted solution of monodisperse particles follows the master equation [27, 28]

$$\frac{d\sigma(q)}{d\Omega(q)} = n\Delta\rho^2 V^2 P(q)S(q), \quad (1)$$

where n is the number of particles, Δρ is the difference in scattering length densities between the particles and the solvent, and V is the specific volume of the particle. P(q) is the form factor, which is a function of the averaged shape and the averaged size of the scattering particles. The effective structure factor is presented in the formula as S(q), which is equal to unity for diluted solutions without interaction between the individual particles.

The pair correlation function P(R) and particle maximum dimension $D_{max}$ were determined by fitting the data using the indirect Fourier transform (IFT) method as implemented in the program GNOM [46].

In case of partial aggregation, the SANS data were fitted using a linear superposition of two intensity profiles: a) the scattering profile of an ellipsoid with uniform scattering length density corresponding to the OCP proteins, and b) a power law

$$I(q)=Aq^{x} \quad (2)$$

representing the scattering from aggregates.

The scattering profile of an ellipsoid with the radii of its three axes being a, b, and c (assuming $a \le b \le c$) and with a uniform scattering length density is given by the equation [47]

$$I(q) = \frac{scale}{V_{el}} \int_0^1 \int_0^1 \phi^2 \left\{ q\left[ a^2 \cos^2\left(\frac{\pi x}{2}\right) + b \sin^2\left(\frac{\pi x}{2}\right)(1-y^2) + c^2 y^2 \right]^{\frac{1}{2}} \right\} dx\,dy, \quad (3)$$

where

$$\phi^2(x) = 9\left( \frac{\sin(x) - x\cos(x)}{x^3} \right)^2 \quad (4)$$

and

$$V_{el} = \frac{4\pi}{3} abc. \quad (5)$$

The global fitting of SANS curves was performed using the SANS software developed at NCNR (NIST) [48].

Low-resolution solution structures were obtained using the ATSAS reconstitution tool DAMMIN developed by the Svergun group based on a reverse Monte Carlo minimization approach [49, 50]. The structural models derived within this study were generally averaged over 20 iterations.

SAXS data were also analyzed using the software package CORAL (COmplexes with RAndom Loops), which allows to define flexible portions in a known crystal structure, while the remaining part of the molecule is modeled as a rigid body [51]. In our analysis, NTD (residues 19-163) and CTD of OCP (residues 171-311) were predefined as rigid bodies based on the 3MG1 pdb code of the $OCP^O$ dimer [18]. In turn, the N-terminal corresponding to the first 18 residues and the linker region (residues 164-170) are assumed to be unfolded and flexible in the Coral analysis.

The CRYSON program [52] was used to calculate theoretical SAXS and SANS curves based on structures (pdb codes) derived from the DAMMIN and CORAL analyses. This is especially useful to compare CORAL structures to SANS data and thus verify their validity, while CORAL is otherwise restricted to the analysis of SAXS data.

## RESULTS AND DISCUSSION

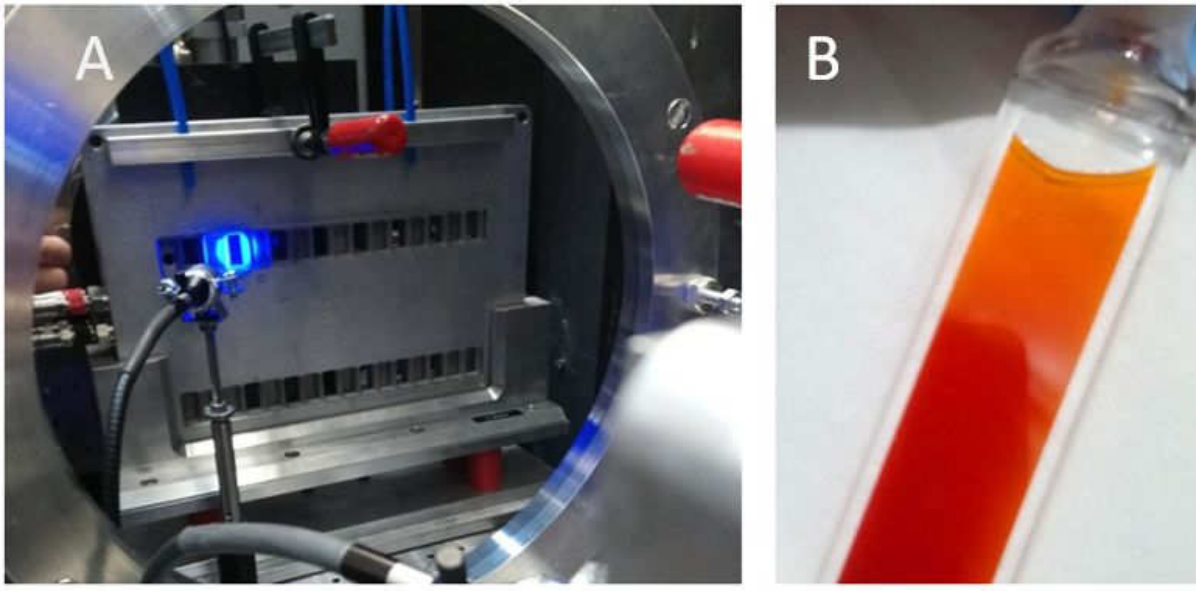


**Figure 2**: SANS experiments of OCP under blue light illumination. A: Illumination setup for OCP at the KWS-1 SANS instrument. B: An OCP sample after SANS experiment with illumination at KWS-1: While the upper non-illuminated part of the sample retains its orange color characteristic for $OCP^O$, the lower illuminated part reveals a color change as expected for $OCP^R$ (illuminated region is indicated by the blue rectangle). Only the lower (illuminated) part of the sample cell is probed in the SANS experiment.

**SANS experiments**: SANS experiments of OCP with and without illumination were carried out at KWS-1. For these experiments the SANS instrument was interfaced with an illumination setup consisting of a laser emitting at 480 nm and a fiber optics to guide the excitation light to the sample (see Fig. 2A). The light intensity was about 5 mW/cm² on the surface of the cuvette. At this intensity a turnover of $OCP^O$ to the active state $OCP^R$ of more than 90% is achieved at 15°C, so that the illuminated part of the sample appeared clearly red, while the non-illuminated part of the sample, which was outside of the neutron beam, remained orange (see Fig. 2B). Consequently, SANS experiments for all samples were carried out at 15°C in order to ensure comparability of the

data. The SANS curves of $OCP^O$ obtained with this setup in the dark (green circles) and of illuminated OCP identified with $OCP^R$ (red squares) at a low protein concentration of about 1 mg/ml are shown in Fig. 3. The two curves exhibit a clear difference in the range of intermediate Q-values. Upon illumination, the curve is shifted towards smaller Q-values indicating an elongation of the OCP molecule in its active state. The SANS data of the $OCP^{W288A}$ mutant obtained for a protein concentration of about 1 mg/ml are also shown in Fig. 3 (cyan triangles). A comparison reveals that the SANS data of $OCP^{W288A}$ are very similar to those of OCP measured under illumination. This finding is in qualitative agreement with the assumption that $OCP^{W288A}$ closely mimics the structure of the active state $OCP^R$. Although the data of $OCP^{W288A}$ are slightly noisier than the other data sets, a small deviation from the $OCP^R$ data is visible in the Q-range between 0.07 and 0.10 $Å^{-1}$. This deviation cannot be attributed to a possibly incomplete turnover of OCP upon illumination, because this effect would lead to a shift of the curve attributed to $OCP^R$ towards higher Q-values, i.e. the opposite of the observed deviation. The data shown in Fig. 3 appear to be free of undesired effects from sample aggregation. This is important since aggregation is known to severely affect spectroscopic properties of pigment-protein complexes[53-55].

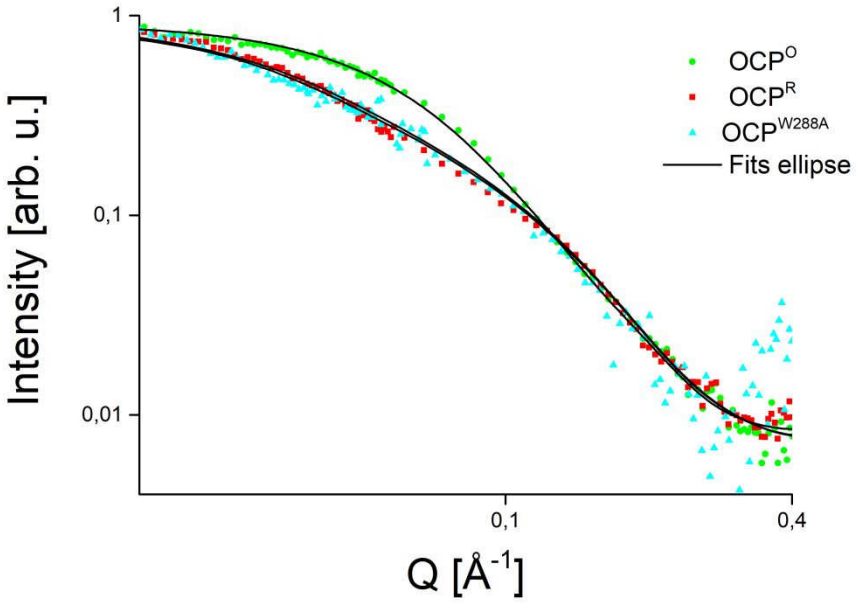


**Figure 3**: SANS data of OCP at a protein concentration of about 1 mg/ml obtained in the dark (green circles) and under constant illumination at 480 nm (red squares), respectively, measured at temperature of 15 °C using the instrument KWS-1. SANS data of OCP$^{W288A}$ measured under the same conditions are shown as cyan triangles. The black solid lines represent the fitting curves of the ellipsoid model (see Table 1).

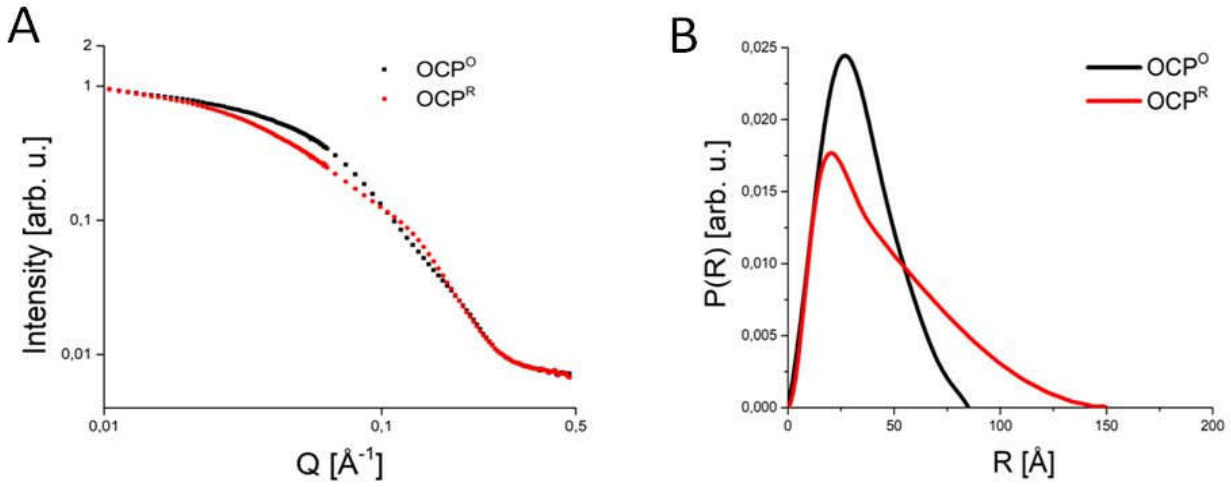


**Figure 4**: A panel: SANS data of OCP at a protein concentration of about 65 mg/ml obtained in the dark (black dots) and under constant illumination at 480 nm (red dots), respectively, measured at temperature of 15 °C using the instrument KWS-1. The experimental error is in the order of the symbol size. B panel: Comparison of P(R) functions calculated from SANS data for OCP$^{O}$ (black line) OCP$^{R}$ (red line) samples.

SANS data for a drastically higher protein concentration of about 65 mg/ml are shown in Fig. 4A for OCP in the dark (black dots) and under constant illumination at 480 nm (red dots) at 15 ºC. These conditions are identical to those employed in neutron spectroscopy to study protein dynamics in the accompanying paper and, thus, characterize the solution structure of the samples used in these complementary experiments. The data shown in Fig. 4A are identical within experimental error to those of the low concentration samples (see Fig. 3). This corroborates that the effect of illumination on the solution structure of OCP remains virtually the same at higher concentration. A very slight increase of SANS intensity towards the lowest Q-values indicates only a small contribution from potential sample aggregation at this very high protein concentration. Overall, the effect of light excitation on the SANS data has a similar qualitative effect as reported previously by Gupta et al. [8], while the effect appears to be more pronounced in Fig. 3 and especially the data of highly concentrated OCP shown in Fig. 4A are characterized by an unparalleled signal-to-noise ratio. This can be mainly attributed to the careful investigation of excitation conditions (see Methods) leading to an almost complete turnover towards $OCP^R$, but also to the high data quality achieved on the KWS-1 SANS instrument.

Based on the SANS data shown in Fig. 4A, the solution structures of OCP in the dark and under illumination can be characterized by the corresponding pair correlation functions P(R) as shown in Fig. 4B. An inspection of these results reveals that OCP elongates towards longer radii upon illumination, while the maximum of the P(R)-function tends towards a slightly smaller value. This indicates that the molecule becomes longer and less compact on one hand, but also looses size in the intermediate dimensions around the maximum of P(R). This is also reflected in the results of a model dependent fit using the shape of an ellipsoid compiled in Table 1. $OCP^O$ is characterized by radii of the ellipsoid of a=9.4 and b=29 Å as well as a radius c=50.8 Å. In contrast, both $OCP^R$ and $OCP^{W288A}$ exhibit a considerably larger radius c of 85 and 92 Å, respectively, but a smaller

dimension of the ellipsoidal radius b on the order of 19 Å. Although the dimensions of radius c appear to be slightly different in $OCP^{R}$ and $OCP^{W288A}$ suggesting a possible structural difference, we note that the values are similar within experimental error, see also data statistics and fit quality in Fig. 3. Structure reconstitutions of $OCP^{R}$ and $OCP^{W288A}$, respectively, are presented below.

**Table 1.** Parameters obtained by fitting the OCP SANS data shown in Fig. 3 (protein concentration of about 1 mg/ml) using an ellipsoid model

| Sample | SANS $OCP^{O}$ | SANS $OCP^{R}$ | SANS $OCP^{W288A}$ |
|---|---|---|---|
| | | | |
| Scaling factor | 0.007±0.0001 | | 0.00034±0.0001 |
| a [Å] | 9.4±1 | 9.1±3 | 8.7±3 |
| b [Å] | 29.0±1 | 18.9±3 | 18.6±3 |
| c [Å] | 50.8±1 | 85.0±5 | 92.0±5 |
| contrast Δρ [1e-6 Å$^2$] | 4.4 | | 4.4 |

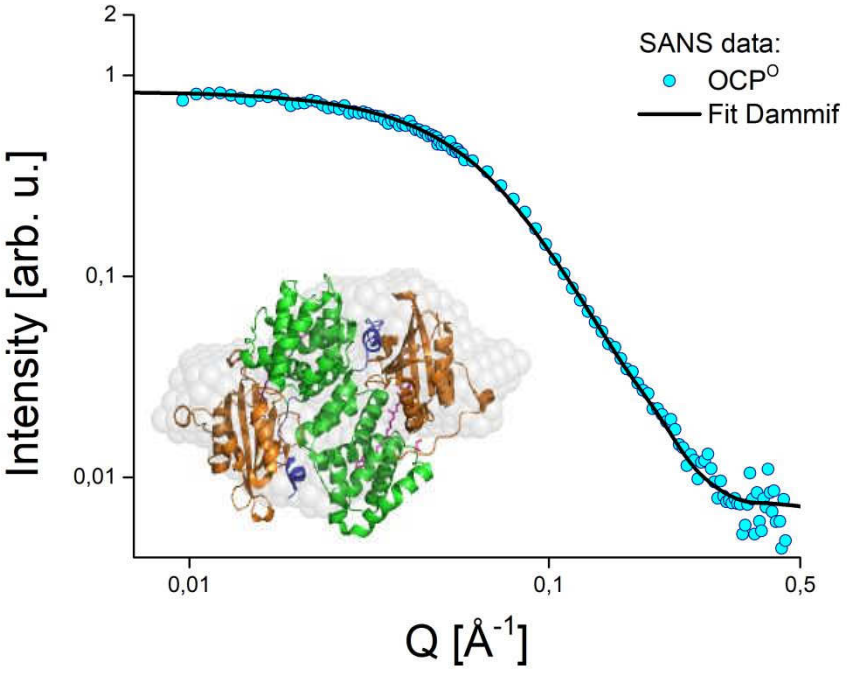


**Figure 5**: Analysis of SANS data of OCP at a protein concentration of about 1 mg/ml measured in the dark at 15 °C (cyan dots): The fit (black line) corresponds to the reconstructed solution structure of OCP (depicted be grey spheres in the inset) obtained using the software package DAMMIF. The crystal structure of dimeric $OCP^O$ by Wilson [18] (PDB-code 3MG1) is shown in the insert for comparison.

**Solution structure of $OCP^O$**: The solution structures of the OCP samples were generally obtained from the SANS data measured at the lowest protein concentration of about 1 mg/ml in order to reduce the influence of protein-protein interactions. This is because effects from protein-protein interactions may be expected at higher concentrations[56, 57]. SANS data of OCP measured in the dark at 15 °C using the instrument KWS-1 are shown as cyan circles in Fig. 5. The solution structure of the sample depicted by grey spheres in the inset of Fig. 5 is reconstituted from the SANS data using the DAMMIN software package (see Table 2 for full set of parameters). The latter structure yields the SANS curve shown as a black line in Fig. 5. The corresponding crystal structure of dimeric OCP is also shown in the inset of Fig. 5, A comparison reveals that the structure reconstituted from the SANS data widely resembles size and shape of an $OCP^O$ dimer suggesting

that the OCP sample is preferentially dimeric. It has to be mentioned that previous studies reported the presence of different OCP oligomers, but especially monomers and dimers, in solution samples [58]. Although this distribution is not visible here, our model has thus to be considered as a minimal description of the SANS data.

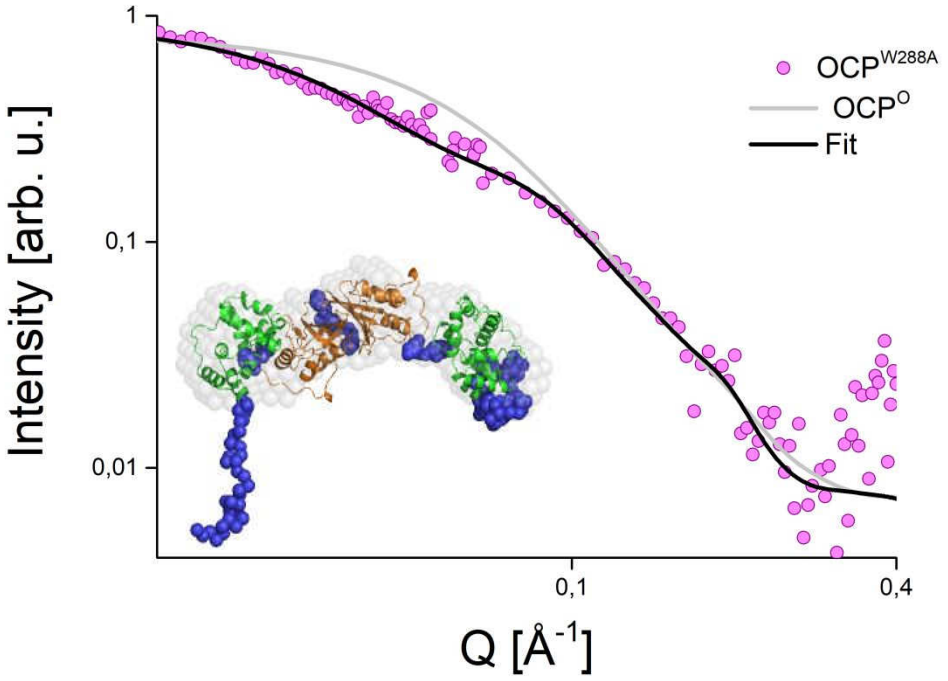


**Figure 6**: Analysis of SANS data of OCP$^{W288A}$ at a protein concentration of about 1 mg/ml measured at 15 °C (purple circles): The fit (black line) corresponds to the reconstructed solution structure of OCP$^{W288A}$ (depicted be grey spheres in the inset) obtained using the software package DAMMIN. The corresponding dimeric structure obtained using CORAL from SAXS data below (see Fig. 9) and identified with OCP$^{R}$ is also shown in the inset. Flexible areas in the OCP structure are indicated in blue, NTD and CTD are shown in green and orange, respectively. For comparison, the grey line shows the SANS curve calculated for an OCP$^{O}$ dimer, see Fig. 5.

**Solution structure of the mutant OCP$^{W288A}$**: As already mentioned in the introduction, OCP$^{W288A}$ is often viewed as a structural analogue of the active state OCP$^{R}$ [59]. The SANS data of the mutant OCP$^{W288A}$ are shown in Fig. 6 by purple circles (see also Fig. 3). For comparison, the fit function determined for OCP$^{O}$ above is also shown as a grey line in Fig. 6, which clearly deviates from the

data. The fit obtained using DAMMIN (see Table 2 for full set of parameters) shows an excellent agreement with the data in Fig. 6 and corresponds to the reconstituted solution structure of the $OCP^{W288A}$ sample given by grey spheres in the inset of Fig. 6. In contrast to the rather compact form of $OCP^{O}$ (see Fig. 5), the reconstituted structure of $OCP^{W288A}$ appears elongated, but slightly narrower. This is the same effect as observed when applying the ellipsoidal model (see Table 1) and consistent with previous studies of $OCP^{W288A}$ [59]. The more detailed structural model shown in the inset of Fig. 6 is obtained using CORAL from SAXS data of $OCP^{W288A}$ and discussed in more detail below. A theoretical SANS curve can be derived from the CORAL structure using the CRYSON routine and yields a fit of the same quality as the black line in Fig. 6 (not shown).

**Solution structure of $OCP^{R}$ obtained by in-situ illumination:** In order to test the expected similarity between the solution structure of $OCP^{W288A}$ on one hand and that of the active state $OCP^{R}$ on the other, we also modeled the SANS data of OCP under illumination shown as green dots in Fig. 7. As outlined above, we achieved a conversion of OCP to $OCP^{R}$ of well above 90% by illumination with blue-light at 15°C (see also Fig. 1 for a picture of the converted sample) so that the sample under study widely reflects $OCP^{R}$. The sample was the same as that used to produce the data of OCP in the dark shown in Fig. 5. For comparison, the fit function of dimeric $OCP^{O}$ is given as a grey line in Fig. 7 (this is the same fit function used for OCP in the dark in Fig. 5). It is apparent that the SANS curve calculated based on the ground state structure of OCP cannot describe the data collected under illumination. In contrast, the fit function obtained by DAMMIN (see Table 2 for full set of parameters) under the same conditions as described above for $OCP^{W288A}$ shows a very good agreement with the experimental data of $OCP^{R}$ (see black line in Fig. 7). That is, the structural model derived for the mutant $OCP^{W288A}$ is also valid for the active state $OCP^{R}$ as achieved by in-situ illumination of an OCP sample. The observation of a generally elongated structure of the

active state of OCP is in agreement with the results of Gupta et al. [8] for monomeric OCP using size exclusion chromatography.

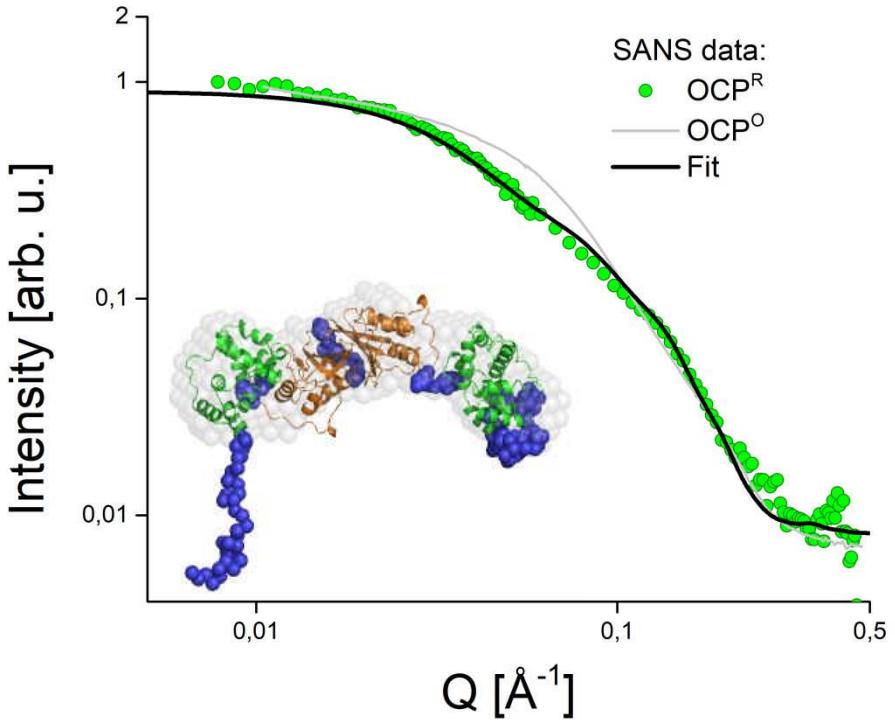


Figure 7: Analysis of SANS data of OCP under illumination at a protein concentration of about 1 mg/ml measured at 15 °C (green dots): The fit (black line) corresponds to the reconstructed solution structure of $OCP^R$ (depicted be grey spheres in the inset) obtained using the software package DAMMIN. The corresponding dimeric structure obtained using CORAL below (see Fig. 9) and identified with $OCP^R$ is also shown in the inset. Flexible areas in the OCP structure are indicated in blue, NTD and CTD are shown in green and orange, respectively. For comparison, the grey line shows the SANS curve calculated for an $OCP^O$ dimer, see Fig. 5.

**Table 2.** Fit parameters obtained from DAMMIN structure reconstructions of SANS data of $OCP^O$ and $OCP^{W288A}$, respectively.

| Fit parameters | $OCP^O$ | $OCP^{W288A}$ | $OCP^R$ |
|---|---|---|---|
| $R_g$ (Å) | 26.6 | 40 | 37.4 |
| $D_{max}$ (Å) | 85 | 170 | 150 |
| $Q_{min}$ ($Å^{-1}$) | 0.01 | 0.01 | 0.01 |
| $Q_{max}$ ($Å^{-1}$) | 0.3 | 0.17 | 0.3 |
| $Chi^2$ | 0.01 | 1.703 | 0.06 |

**Solution structures at high protein concentration verified by SANS and SAXS:** As pointed out in the Introduction, the active state $OCP^R$ may not only be characterized by a specific structure, but also by a high degree of molecular flexibility referred to as a "molten globule state". Protein dynamics/flexibility can be directly investigated by neutron spectroscopy as demonstrated for OCP in the accompanying paper [60]. As a general drawback, neutron spectroscopy requires a rather high protein concentration of > 50mg/ml in order to increase the contribution of protein scattering compared with that of the solvent. Such conditions may lead to formation of higher oligomers [22, 58] or even significant non-systematic sample aggregation. In turn, the sample structure may be significantly affected so that the measured dynamics cannot be unambiguously related to the inferred structures of the ground and active states of OCP, respectively. Therefore, the solution structures of the OCP and $OCP^{W288A}$ samples employed for QENS were verified using SANS and SAXS, respectively. SANS data of OCP measured using the instrument KWS-1 at a protein concentration of about 65 mg/ml and at a temperature of 15 °C are shown as blue dots in Fig. 8. The data were fitted using the reconstituted structure of dimeric $OCP^O$ obtained at low

concentration above (see black line in Fig. 5), which results in the red line in Fig. 7. In addition, a power law representing a minor fraction of aggregates (blue line) has to be taken into account to describe the data. The full fit is shown as a black line in Fig. 8. Thus, it can be concluded that the OCP sample for QENS experiments is preferentially dimeric (grey spheres in Fig. 5) and only slightly affected by aggregation despite of the relatively high protein concentration.

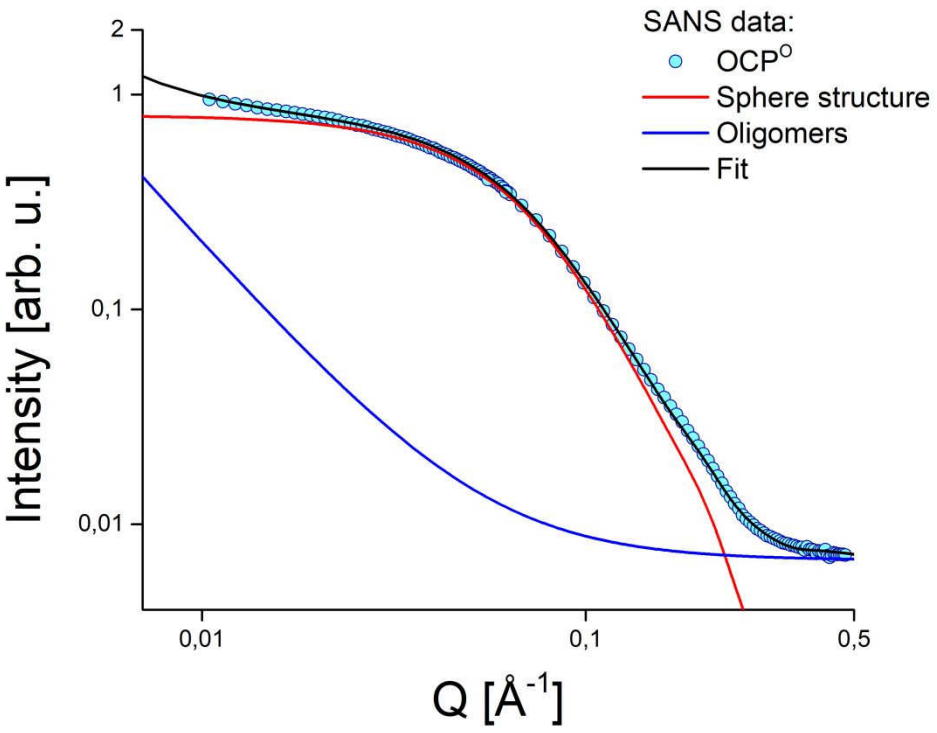


**Figure 8**: Verification of the solution structure of the OCP sample at a protein concentration of about 65 mg/ml using SANS data measured at 15 °C (blue circles). The fit (black line) was obtained as the sum of the reconstructed solution structure of OCP (red line) using the software package DAMMIF (see Fig. 5) and a power law accounting for aggregation (blue line).

In a first attempt of QENS experiments on OCP, $OCP^{W288A}$ will be used as a structural analogue of the active state $OCP^{R}$. SAXS data of $OCP^{W288A}$ measured at a protein concentration of about 65 mg/ml at 20 °C are shown as green points in Fig. 9. The SAXS data of $OCP^{W288A}$ were fitted using the same dimeric model as shown in Fig. 6 (see black line in Fig. 9) for the mutant sample at

a protein concentration of 1 mg/ml exhibiting the expected elongated structure. This confirms that the $OCP^{W288A}$ sample prepared for QENS is virtually free of aggregation and corresponds to the active state structure $OCP^{R}$, i.e. the samples can be used for neutron spectroscopy and the measured molecular dynamics can be related to the above solution structures.

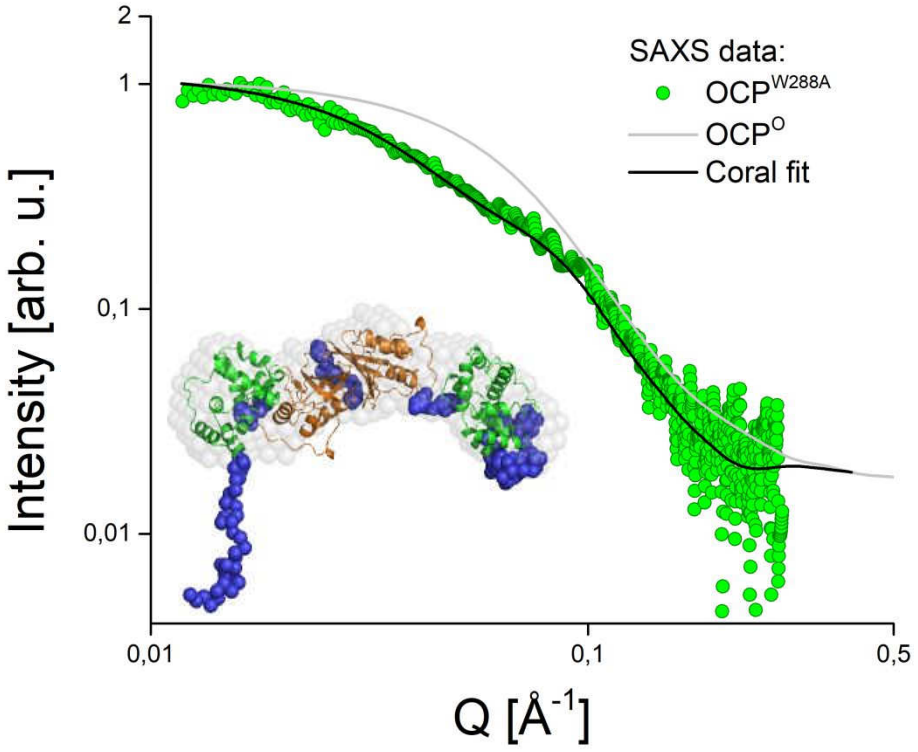


Figure 9: Verification of the solution structure of $OCP^{W288A}$ at a protein concentration of about 65 mg/ml using SAXS data (green circles). The fit (black line) was obtained according to the CORAL structure of $OCP^{R}$ shown in Figs. 5 and 6. For comparison, the grey line shows the fit function of $OCP^{O}$ shown in Fig. 5.

CORAL structural model of $OCP^{R}$: In order to achieve a better impression of the structural changes, we also modelled the SAXS data of $OCP^{W288A}$ using the CORAL routine. This package can be used for SAXS data only and allows defining flexible and rigid domains of the known crystal structure of dimeric OCP (Wilson et al. [18], PDB-code 3MG1), respectively, whose arrangement is subsequently optimized to yield the best fit of the experimental data (see Methods). In our analysis, NTD (residues 19-163) and CTD of OCP (residues 171-311) were predefined as rigid bodies based

on the 3MG1 pdb code of the $OCP^O$ dimer[18]. In turn, the N-terminal corresponding to the first 18 residues and the linker region (residues 164-170) are assumed to be unfolded and flexible in the Coral analysis. This approach is very similar to those used before for OCP [8] and $OCP^{W288A}$ [10]. Following Maksimov et al. [59], however, the two OCP molecules of the dimer are associated via their CTDs (see orange structure in Fig.1). This assumption is based on the observation that separate CTDs form dimers in solution, while dimerization is not observed for NTDs. A similar association of the two monomers is reported more recently by Harris et al.[61]. Furthermore, the structures of the two OCPs within the dimer are optimized independently, i.e. no assumptions about the symmetry of the dimer are imposed. Since SANS is a low-resolution technique, the location of the chromophore is not considered in the models presented here.

Since the crystal structure of $OCP^O$ suggests dimerization via NTDs in the inactive ground state of OCP, an association of $OCP^R$ dimers via their CTDs appears surprising at first glance. However, there are a number of arguments which support the structural organization of $OCP^R$ as shown in Fig. 9: i) a CORAL model of $OCP^R$ assuming association via NTDs (not shown) consistently exhibits the same basic features like domain separation and NTE unfolding as the model shown in Fig. 9, but has a higher $Chi^2$-value and is thus less probable, ii) the interaction between $OCP^O$ monomers appears to be weak and relies on a few charged protein residues only, which are - according to X-ray crystal structure information[62] – present in dimer-forming representatives of the OCP1 clade, but absent in members of the OCP2 clade occurring only as a monomer[62], and iii) thus, it is a speculative but reasonable argument to assume that the light-induced structural changes within the NTD affect the weak association of the monomeric subunits via their NTDs and lead to a rearrangement of the dimer association as well. The latter assumption is also consistent with rather long conversion times to $OCP^R$ [16], which should allow large scale structural rearrangements within OCP itself, but also within the OCP dimer.

The CORAL fit is shown as a black line in Fig. 9 and provides an excellent agreement with the SAXS data set. A comparison of the obtained structure (see inset of Fig. 9) with the reconstitution obtained above by DAMMIN (see Fig. 6) also reveals a good agreement except for the highly flexible NTE. This is not surprising as the reconstruction tool DAMMIN is intended for application to compact molecular shapes. The optimized structure of $OCP^{W288A}$ reveals all expected features of the active state $OCP^{R}$ [8, 10] like: i) separation of the two domains resulting in a generally elongated structure, and ii) unfolding of the NTE thus becoming a highly flexible entity (see especially the OCP monomer to the left in the inset of Fig. 9). The difference between the two OCP monomers shown in Fig. 9 can be viewed as a measure for the flexibility of the $OCP^{R}$ structure allowed within the experimental uncertainty of the SANS data.

## Conclusions

As pointed out in the introduction, crystal structures of the active state $OCP^{R}$ are not yet available. In this regard, small-angle scattering methods combined with simulation software like the reconstruction tool DAMMIN and optimization routine CORAL for flexible structures, respectively, are valuable experimental tools to determine low-resolution structures in aqueous solution. In addition, SANS structures are obtained in solution and thus under widely identical conditions used for spectroscopic experiments to investigate the function of OCP. In summary, we confirm that the structure of the active state $OCP^{R}$ is characterized by the separation of the two domains NTD and CTD resulting in an extended structure along with unfolding of the NTE. The NTE appears to be highly flexible allowing various local conformations. Our results largely corroborate those of [8, 10] for the cases of $OCP^{R}$ and $OCP^{W288A}$, respectively. However, we can directly compare the latter to the solution structure of $OCP^{R}$ induced by in-situ illumination thus

confirming that $OCP^{W288A}$ can be used as a structural analogue of the active state $OCP^{R}$. We can also confirm that the latter active state structures remain largely valid for samples at high protein concentrations of >50 mg/ml as used for neutron spectroscopy experiments on protein dynamics in the accompanying paper.

## Acknowledgement

Financial Support by the Estonian Research Council (Grants PRG 539 and SLOKT 12026 T) is gratefully acknowledged. J.P. is also deeply indebted to the European Social Fund's Internationalisation Programme DoRa for financial support. We also thank JCNS and MLZ Garching, Germany for the allocation of beamtime, and for technical support when using the custom-built illumination setup at KWS-1. F.-J.S. acknowledges financial support by BMBF (FKZ 01DJ15007) as well as COST MP1205.

References:

1. El Bissati, K.; Delphin, E.; Murata, N.; Etienne, A.; Kirilovsky, D. Photosystem Ii Fluorescence Quenching in the Cyanobacterium Synechocystis Pcc 6803: Involvement of Two Different Mechanisms. Biochim. Biophys. Acta **2000,** *1457*, 229-242.
2. Gwizdala, M.; Wilson, A.; Kirilovsky, D. In Vitro Reconstitution of the Cyanobacterial Photoprotective Mechanism Mediated by the Orange Carotenoid Protein in Synechocystis Pcc 6803. Plant Cell **2011,** *23*, 2631-2643.
3. Kirilovsky, D.; Kerfeld, C. A. The Orange Carotenoid Protein in Photoprotection of Photosystem Ii in Cyanobacteria. Biochim. Biophys. Acta **2012,** *1817*, 158-166.
4. Maksimov, E. G.; Schmitt, F. J.; Shirshin, E. A.; Svirin, M. D.; Elanskaya, I. V.; Friedrich, T.; Fadeev, V. V.; Paschenko, V. Z.; Rubin, A. B. The Time Course of Non-Photochemical Quenching in Phycobilisomes of Synechocystis Sp. Pcc6803 as Revealed by Picosecond Time-Resolved Rluorimetry. Biochim. Biophys. Acta **2014,** *1837*, 1540-1547.
5. Wilson, A.; Punginelli, C.; Gall, A.; Bonetti, C.; Alexandre, M.; Routaboul, J. M.; Kerfeld, C. A.; van Grondelle, R.; Robert, B.; Kennis, J. T., et al. A Photoactive Carotenoid Protein Acting as Light Intensity Sensor. Proc. Natl. Acad. Sci. U. S. A. **2008,** *105*, 12075-12080.
6. Squires, A. H.; Dahlberg, P. D.; Liu, H.; Magdaong, N. C. M.; Blankenship, R. E.; Moerner, W. E. Single-Molecule Trapping and Spectroscopy Reveals Photophysical Heterogeneity of Phycobilisomes Quenched by Orange Carotenoid Protein. Nat. Commun. **2019,** *10*, 1-12.
7. Kerfeld, C. A.; Sawaya, M. R.; Brahmandam, V.; Cascio, D.; Ho, K. K.; Trevithick-Sutton, C. C.; Krogmann, D. W.; Yeates, T. O. The Crystal Structure of a Cyanobacterial Water-Soluble Carotenoid Binding Protein. Structure **2003,** *11*, 55-65.
8. Gupta, S.; Guttman, M.; Leverenz, R. L.; Zhumadilova, K.; Pawlowski, E. G.; Petzold, C. J.; Lee, K. K.; Ralston, C. Y.; Kerfeld, C. A. Local and Global Structural Drivers for the Photoactivation of the Orange Carotenoid Protein. Proc. Natl. Acad. Sci. U. S. A. **2015,** *112*, 5567-5574.
9. Punginelli, C.; Wilson, A.; Routaboul, J. M.; Kirilovsky, D. Influence of Zeaxanthin and Echinenone Binding on the Activity of the Orange Carotenoid Protein. Biochim. Biophys. Acta **2009,** *1787*, 280-188.
10. Maksimov, E. G.; Sluchanko, N. N.; Slonimskiy, Y. B.; Slutskaya, E. A.; Stepanov, A. V.; Argentova-Stevens, A. M.; Shirshin, E. A.; Tsoraev, G. V.; Klementiev, K. E.; Slatinskaya, O. V., et al. The Photocycle of Orange Carotenoid Protein Conceals Distinct Intermediates and Asynchronous Changes in the Carotenoid and Protein Components. Sci. Rep. **2017,** *7*, 1-12.

11. Maksimov, E. G.; Shirshin, E. A.; Sluchanko, N. N.; Zlenko, D. V.; Parshina, E. Y.; Tsoraev, G. V.; Klementiev, K. E.; Budylin, G. S.; Schmitt, F. J.; Friedrich, T., et al. The Signaling State of Orange Carotenoid Protein. Biophys. J. **2015,** *109*, 595-607.
12. Boulay, C.; Wilson, A.; D'Haene, S.; Kirilovsky, D. Identification of a Protein Required for Recovery of Full Antenna Capacity in Ocp-Related Photoprotective Mechanism in Cyanobacteria. Proc. Natl. Acad. Sci. U. S. A. **2010,** *107*, 11620-11625.
13. Gwizdala, M.; Wilson, A.; Omairi-Nasser, A.; Kirilovsky, D. Characterization of the Synechocystis Pcc 6803 Fluorescence Recovery Protein Involved in Photoprotection. Biochim. Biophys. Acta **2013,** *1827*, 348-354.
14. Maksimov, E. G.; Klementiev, K. E.; Shirshin, E. A.; Tsoraev, G. V.; Elanskaya, I. V.; Paschenko, V. Z. Features of Temporal Behavior of Fluorescence Recovery in Synechocystis Sp. Pcc6803. Photosynth. Res. **2015,** *125*, 167-178.
15. Sluchanko, N. N.; Slonimskiy, Y. B.; Shirshin, E. A.; Moldenhauer, M.; Friedrich, T.; Maksimov, E. G. Ocp-Frp Protein Complex Topologies Suggest a Mechanism for Controlling High Light Tolerance in Cyanobacteria. Nat. Commun. **2018,** 9, 1-15.
16. Sluchanko, N. N.; Klementiev, K. E.; Shirshin, E. A.; Tsoraev, G. V.; Friedrich, T.; Maksimov, E. G. The Purple Trp288ala Mutant of Synechocystis Ocp Persistently Quenches Phycobilisome Fluorescence and Tightly Interacts with Frp. Biochim. Biophys. Acta, Bioenerg. **2017,** *1858*, 1-11.
17. Leverenz, R. L.; Sutter, M.; Wilson, A.; Gupta, S.; Thurotte, A.; Bourcier de Carbon, C.; Petzold, C. J.; Ralston, C.; Perreau, F.; Kirilovsky, D., et al. Photosynthesis. A 12 a Carotenoid Translocation in a Photoswitch Associated with Cyanobacterial Photoprotection. Science **2015,** *348*, 1463-1466.
18. Wilson, A.; Kinney, J. N.; Zwart, P. H.; Punginelli, C.; D'Haene, S.; Perreau, F.; Klein, M. G.; Kirilovsky, D.; Kerfeld, C. A. Structural Determinants Underlying Photoprotection in the Photoactive Orange Carotenoid Protein of Cyanobacteria. J. Biol. Chem. **2010,** *285*, 18364-18375.
19. Thurotte, A.; Lopez-Igual, R.; Wilson, A.; Comolet, L.; Bourcier de Carbon, C.; Xiao, F.; Kirilovsky, D. Regulation of Orange Carotenoid Protein Activity in Cyanobacterial Photoprotection. Plant Physiol. **2015,** *169*, 737-747.
20. Zhang, H.; Liu, H.; Lu, Y.; Wolf, N. R.; Gross, M. L.; Blankenship, R. E. Native Mass Spectrometry and Ion Mobility Characterize the Orange Carotenoid Protein Functional Domains. Biochim. Biophys. Acta **2016,** *1857*, 734-739.
21. Wilson, A.; Punginelli, C.; Couturier, M.; Perreau, F.; Kirilovsky, D. Essential Role of Two Tyrosines and Two Tryptophans on the Photoprotection Activity of the Orange Carotenoid Protein. Biochim. Biophys. Acta **2011,** *1807*, 293-301.
22. Maksimov, E. G.; Moldenhauer, M.; Shirshin, E. A.; Parshina, E. A.; Sluchanko, N. N.; Klementiev, K. E.; Tsoraev, G. V.; Tavraz, N. N.; Willoweit, M.;

Schmitt, F. J., et al. A Comparative Study of Three Signaling Forms of the Orange Carotenoid Protein. Photosynth. Res. **2016,** *130*, 389-401.
23. Bandara, S.; Ren, Z.; Lu, L.; Zeng, X.; Shin, H.; Zhao, K. H.; Yang, X. Photoactivation Mechanism of a Carotenoid-Based Photoreceptor. Proc. Natl. Acad. Sci. U. S. A. **2017,** *114*, 6286-6291.
24. Konold, P. E.; van Stokkum, I. H. M.; Muzzopappa, F.; Wilson, A.; Groot, M. L.; Kirilovsky, D.; Kennis, J. T. M. Photoactivation Mechanism, Timing of Protein Secondary Structure Dynamics and Carotenoid Translocation in the Orange Carotenoid Protein. J. Am. Chem. Soc. **2019,** *141*, 520-530.
25. Kirilovsky, D.; Kerfeld, C. A. Cyanobacterial Photoprotection by the Orange Carotenoid Protein. Nat. Plants **2016,** *2*, 1-7.
26. Maksimov, E. G.; Sluchanko, N. N.; Mironov, K. S.; Shirshin, E. A.; Klementiev, K. E.; Tsoraev, G. V.; Moldenhauer, M.; Friedrich, T.; Los, D. A.; Allakhverdiev, S. I., et al. Fluorescent Labeling Preserving Ocp Photoactivity Reveals Its Reorganization During the Photocycle. Biophys. J. **2017,** *112*, 827.
27. Jacques, D. A.; Trewhella, J. Small-Angle Scattering for Structural Biology - Expanding the Frontier While Avoiding the Pitfalls. Protein Sci. **2010,** *19*, 642-657.
28. Kikhney, A. G.; Svergun, D. I. A Practical Guide to Small Angle X-Ray Scattering (Saxs) of Flexible and Intrinsically Disordered Proteins. FEBS Lett. **2015,** *589*, 2570-2577.
29. Kühn, P.; Pieper, J.; Kaminskaya, O.; Eckert, H. J.; Lechner, R. E.; Shuvalov, V.; Renger, G. Reaction Pattern of Photosystem Ii: Oxidative Water Cleavage and Protein Flexibility. Photosynth. Res. **2005,** *84*, 317-323.
30. Pieper, J.; Renger, G. Protein Dynamics Investigated by Neutron Scattering. Photosynth. Res. **2009,** *102*, 281-293.
31. Pieper, J.; Trapp, M.; Skomorokhov, A.; Natkaniec, I.; Peters, J.; Renger, G. Temperature-Dependent Vibrational and Conformational Dynamics of Photosystem Ii Membrane Fragments from Spinach Investigated by Elastic and Inelastic Neutron Scattering. Biochim. Biophys. Acta, Bioenerg. **2012,** *1817*, 1213-1219.
32. Golub, M.; Combet-Jeancenel, S.; Lairez, D.; Wieland, F.; Soloviov, D.; Kuklin, A.; Lokstein, H.; Schmitt, F. J.; Hecht, M.; Eckert, H. J., et al. Solution Structure and Excitation Energy Transfer in Phycobiliproteins of Acaryochloris Marina Investigated by Small Angle Scattering. Biochim. Biophys. Acta **2017,** *1858*, 318-324.
33. Tiede, D. M.; Littrell, K.; Marone, P. A.; Zhang, R.; Thiyagarjan, P. Solution Structure of a Biological Bimolecular Electron Transfer Complex: Characterization of the Photosynthetic Reaction Center-Cytochrome C2 Protein Complex by Small Angle Neutron Scattering. J. Appl. Crystallogr. **2000,** *33*, 560-564.
34. Golub, M.; Hejazi, M.; Kolsch, A.; Lokstein, H.; Wieland, D. C.; Zouni, A.; Pieper, J. Solution Structure of Monomeric and Trimeric Photosystem I of

Thermosynechococcus Elongatus Investigated by Small-Angle X-Ray Scattering. Photosynth. Res. **2017,** *133*, 163-173.
35. Cardoso, M. B.; Smolensky, D.; Heller, W. T.; O'Neill, H. Insight into the Structure of Light-Harvesting Complex Ii and Its Stabilization in Detergent Solution. J. Phys. Chem. B **2009,** *113*, 16377-16383.
36. Nagy, G.; Garab, G.; Pieper, J., Neutron Scattering in Photosynthesis Research. In Contemporary Problems of Photosynthesis Allakhverdiev, S.; Rubin, A. B.; Shuvalov, V. A., Eds. Institute of Computer Science: Izhevsk, 2014; Vol. 1, pp 69-121.
37. Nagy, G.; Posselt, D.; Kovacs, L.; Holm, J. K.; Szabo, M.; Ughy, B.; Rosta, L.; Peters, J.; Timmins, P.; Garab, G. Reversible Membrane Reorganizations During Photosynthesis in Vivo: Revealed by Small-Angle Neutron Scattering. Biochem. J. **2011,** *436*, 225-230.
38. Kirkensgaard, J. J. K.; Holm, J. K.; Larsen, J. K.; Posselt, D. Simulation of Small-Angle X-Ray Scattering from Thylakoid Membranes. J. Appl. Crystallogr. **2009,** *42*, 649-659.
39. Pieper, J.; Rusevich, L.; Hauss, T.; Renger, G. Lamellar Spacing of Photosystem Ii Membrane Fragments Upon Dehydration Studied by Neutron Membrane Diffraction. Optofluid **2015,** *2*, 36-40.
40. Liberton, M.; Page, L. E.; O'Dell, W. B.; O'Neill, H.; Mamontov, E.; Urban, V. S.; Pakrasi, H. B. Organization and Flexibility of Cyanobacterial Thylakoid Membranes Examined by Neutron Scattering. J. Biol. Chem. **2013,** *2*88, 3632-3640.
41. Li, Y.; Lin, Y.; Garvey, C. J.; Birch, D.; Corkery, R. W.; Loughlin, P. C.; Scheer, H.; Willows, R. D.; Chen, M. Characterization of Red-Shifted Phycobilisomes Isolated from the Chlorophyll F-Containing Cyanobacterium Halomicronema Hongdechloris. Biochim. Biophys. Acta **2016,** *1*857, 107-114.
42. Nagy, G.; Unnep, R.; Zsiros, O.; Tokutsu, R.; Takizawa, K.; Porcar, L.; Moyet, L.; Petroutsos, D.; Garab, G.; Finazzi, G., et al. Chloroplast Remodeling During State Transitions in Chlamydomonas Reinhardtii as Revealed by Noninvasive Techniques in Vivo. Proc. Natl. Acad. Sci. U. S. A. **2014,** *111*, 5042-5047.
43. Tyler, R. C.; Sreenath, H. K.; Singh, S.; Aceti, D. J.; Bingman, C. A.; Markley, J. L.; Fox, B. G. Auto-Induction Medium for the Production of [U-15n]- and [U-13c, U-15n]-Labeled Proteins for Nmr Screening and Structure Determination. Protein Expression Purif. **2005,** *40*, 268-278.
44. Pipich, V. Qtikws. www.qtikws.de (accessed Oct 3, 2017).
45. Feoktystov, A.; Frielinghaus, H.; Di, Z.; Jaksch, S.; Pipich, V.; Appavou, M.-S.; Babcock, E.; Hanslik, R.; Engels, R.; Kemmerling, G., et al. Kws-1 High-Resolution Small-Angle Neutron Scattering Instrument at Jcns: Current State. J. Appl. Crystallogr. **2015,** *4*8, 61-70.

46. Svergun, D. I. Determination of the Regularization Parameter in Indirect-Transform Methods Using Perceptual Criteria. J. Appl. Crystallogr. **1992,** *25*, 495-503.
47. Feigin, L. A.; Svergun, D. I. Structure Analysis by Small-Angle X-Ray and Neutron Scattering. Plenum Press: New York, 1987.
48. Kline, S. R. Reduction and Analysis of Sans and Usans Data Using Igor Pro. J. Appl. Crystallogr. **2006,** *39*, 895-900.
49. Franke, D.; Svergun, D. I. Dammif, a Program for Rapid Ab-Initio Shape Determination in Small-Angle Scattering. J. Appl. Crystallogr. **2009,** *42*, 342-346.
50. Konarev, P. V.; Volkov, V. V.; Sokolova, A. V.; Koch, M. H. J.; Svergun, D. I. Primus: A Windows Pc-Based System for Small-Angle Scattering Data Analysis. J. Appl. Crystallogr. **2003,** *36*, 1277-1282.
51. Petoukhov, M. V.; Franke, D.; Shkumatov, A. V.; Tria, G.; Kikhney, A. G.; Gajda, M.; Gorba, C.; Mertens, H. D.; Konarev, P. V.; Svergun, D. I. New Developments in the Atsas Program Package for Small-Angle Scattering Data Analysis. J. Appl. Crystallogr. **2012,** *45*, 342-350.
52. Svergun, D. I.; Barberato, C.; Koch, M. H. J. Crysol - a Program to Evaluate X-Ray Solution Scattering of Biological Macromolecules Form Atomic Coordinates. J. Appl. Crystallogr. **1995,** *28*, 768-773.
53. Vasilev, S.; Irrgang, K. D.; Schrotter, T.; Bergmann, A.; Eichler, H. J.; Renger, G. Quenching of Chlorophyll Alpha Fluorescence in the Aggregates of Lhcii: Steady State Fluorescence and Picosecond Relaxation Kinetics. Biochemistry **1997,** *36*, 7503-7512.
54. Pieper, J.; Irrgang, K. D.; Rätsep, M.; Jankowiak, R.; Schrotter, T.; Voigt, J.; Small, G. J.; Renger, G. Effects of Aggregation on Trimeric Light-Harvesting Complex Ii of Green Plants: A Hole-Burning Study. J. Phys. Chem. A **1999,** *103*, 2422-2428.
55. Enriquez, M. M.; Akhtar, P.; Zhang, C.; Garab, G.; Lambrev, P. H.; Tan, H. S. Energy Transfer Dynamics in Trimers and Aggregates of Light-Harvesting Complex Ii Probed by 2d Electronic Spectroscopy. J. Phys. Chem. **2015,** *142*, 1-10.
56. Ameseder, F.; Radulescu, A.; Holderer, O.; Falus, P.; Richter, D.; Stadler, A. M. Relevance of Internal Friction and Structural Constraints for the Dynamics of Denatured Bovine Serum Albumin. J. Phys. Chem. Lett. **2018,** 9, 2469-2473.
57. Ameseder, F.; Biehl, R.; Holderer, O.; Richter, D.; Stadler, A. M. Localised Contacts Lead to Nanosecond Hinge Motions in Dimeric Bovine Serum Albumin. Phys. Chem. Chem. Phys. **2019**, 1-9.
58. Lu, Y.; Liu, H.; Saer, R. G.; Zhang, H.; Meyer, C. M.; Li, V. L.; Shi, L.; King, J. D.; Gross, M. L.; Blankenship, R. E. Native Mass Spectrometry Analysis of Oligomerization States of Fluorescence Recovery Protein and Orange Carotenoid Protein: Two Proteins Involved in the Cyanobacterial Photoprotection Cycle. Biochemistry **2017,** *56*, 160-166.

59. Maksimov, E. G.; Sluchanko, N. N.; Slonimskiy, Y. B.; Mironov, K. S.; Klementiev, K. E.; Moldenhauer, M.; Friedrich, T.; Los, D. A.; Paschenko, V. Z.; Rubin, A. B. The Unique Protein-to-Protein Carotenoid Transfer Mechanism. Biophys. J. **2017,** *113*, 402-414.
60. Golub, M.; Moldenhauer, M.; Schmitt, F. J.; Lohstroh, W.; Maksimov, E. G.; Friedrich, T.; Pieper, J. Solution Structure and Conformational Fexibility in the Active State of the Orange Carotenoid Protein: Part Ii: Quasielastic Neutron Scattering J. Phys. Chem. B submitted.
61. Harris, D.; Wilson, A.; Muzzopappa, F.; Sluchanko, N. N.; Friedrich, T.; Maksimov, E. G.; Kirilovsky, D.; Adir, N. Structural Rearrangements in the C-Terminal Domain Homolog of Orange Carotenoid Protein Are Crucial for Carotenoid Transfer. Commun. Biol. **2018,** *1*, 1-25.
62. Bao, H.; Melnicki, M. R.; Pawlowski, E. G.; Sutter, M.; Agostoni, M.; Lechno-Yossef, S.; Cai, F.; Montgomery, B. L.; Kerfeld, C. A. Additional Families of Orange Carotenoid Proteins in the Photoprotective System of Cyanobacteria. Nat. Plants **2017,** *3*, 17089.

TOC graphics